PHYSICAL REVIEW B **88**, 144427 (2013)

Inducing exchange bias in $La_{0.67}Sr_{0.33}MnO_{3-\delta}/SrTiO_3$ thin films by strain and oxygen deficiency

D. Schumacher, A. Steffen, J. Voigt, J. Schubert, and Th. Brückel
Jülich Center for Neutron Science JCNS and Peter Grünberg Institut PGI, JARA-FIT, and Forschungszentrum Jülich GmbH, 52425 Jülich, Germany

H. Ambaye and V. Lauter
Spallation Neutron Source, Neutron Science Directorate, Oak Ridge National Laboratory, Oak Ridge, Tennessee 37831, USA
(Received 14 December 2012; revised manuscript received 24 July 2013; published 31 October 2013)

We present an exchange bias (EB) effect of variable size in $La_{0.67}Sr_{0.33}MnO_{3-\delta}$ single and $La_{0.67}Sr_{0.33}MnO_{3-\delta}/SrTiO_3$ (LSMO/STO) bilayers grown on STO substrates. Samples have been prepared by pulsed laser deposition (PLD) and high-pressure sputter deposition (HSD) in oxygen atmosphere at different oxygen pressures. Increased out-of-plane lattice parameters of the LSMO layers and reduced Curie temperatures indicate oxygen deficiencies in the samples grown at lower oxygen pressures. We found an increase of the EB and the coercive fields with decreasing oxygen pressure, whereas the growth at high pressures does not lead to an EB effect. The depth-sensitive method of polarized neutron reflectometry (PNR) reveals a region with drastically reduced, maybe even completely vanishing net magnetization in the LSMO layer at the interface to STO in the exchange-biased samples, but not in the non-exchanged-biased one. It is suggested that an antiferromagnetic structure is formed in this part of the LSMO thin film, which causes the EB effect in this system. An explanation based on the strain-doping phase diagram of LSMO is provided. Thus our findings open a route for tuning the EB effect by changing the oxygen vacancy concentrations.

DOI: 10.1103/PhysRevB.88.144427 PACS number(s): 75.70.Cn

I. INTRODUCTION

One of the main challenges of modern condensed matter research is the preparation, analysis, and understanding of strongly correlated electron systems in complex oxides.[1] The ground state of these fascinating materials is determined by the interplay of lattice, charge, spin, and orbital degrees of freedom. Therefore, a huge variety of extraordinary properties have already been discovered in oxide materials, such as colossal magnetoresistance (CMR) in manganites such as $La_{0.67}Sr_{0.33}MnO_3$ (Ref. 2) or high-T_C superconductivity.[3] Due to recent improvements in thin-film deposition techniques such as high-pressure sputter deposition (HSD), pulsed laser deposition (PLD), and oxidic molecular beam epitaxy, combining two materials with different properties in a thin-film system can lead to even more interesting and novel effects due to the coupling of the different properties via the common interface or the additional lattice strain present at the interface—or a combination of both. One of the best-known combinations is the preparation of an interface between an antiferromagnet and a ferromagnet, which in many cases causes an exchange bias (EB) effect in the system, i.e., a shift of the hysteresis curve along the field axis. Although the EB effect is known for a few decades,[4] the different occurrences of the EB effect[5,6] continue to fascinate. While EB effects have been established in numerous metallic systems, using it in oxide systems opens the perspective of combining the EB effect with other emerging functions. As an example, switching between the two distinct EB states by reversing the polarization of $BiFeO_3$ has been realized in $BiFeO_3/La_{0.67}Sr_{0.33}MnO_3$ thin films,[7] showing the importance of the EB effect for possible device applications and the necessity of a better understanding of the effect.

Out of the large group of strongly correlated oxides, $La_{1-x}Sr_xMnO_3$ (LSMO) is one of the most-studied bulk materials due to the CMR effect and the huge variety of magnetic properties, which exist by changing the doping level.[8] Whereas a phase diagram for the bulk has already been established some time ago,[8] the new properties and phenomena arise in thin LSMO films depending on stoichiometry and strain.[9] For example, a new magnetic configuration in an LSMO thin film deposited on $SrTiO_3$ (STO) has been found by x-ray magnetic circular dichroism (XMCD) (Ref. 10) recently. Besides changing the La/Sr ratio, the charge-carrier density in LSMO can also be influenced by varying the oxygen stoichiometry. The magnetoresistive properties of oxygen-deficient LSMO and how they depend on the oxygen content have already been studied extensively.[11]

An EB has been observed in a LSMO/STO multilayer by Zhu *et al.*[12–14] It was proposed that a disordered spin state at the interface creates the EB caused by the strain exerted by the STO. A vertical shift of the hysteresis loops along the magnetization axis was proposed as an indirect hint supporting this assumption. Here we report on a tunable EB effect in LSMO single layers and LSMO/STO bilayers deposited on STO substrates. Our macroscopic magnetic characterization and x-ray diffraction measurements suggest a correlation between oxygen deficiency and the EB effect: We find an increasing EB effect, i.e., an increasing shift of the hysteresis curves, with increasing oxygen deficiencies, while no EB effect is detected in samples with a stoichiometric $La_{0.67}Sr_{0.33}MnO_3$ film. The size of the EB is influenced by changing the oxygen pressure in the HSD chamber during preparation. Using the depth sensitive technique of polarized neutron reflectometry (PNR) we detected a region of at least drastically reduced, maybe even completely vanishing net magnetization in the exchange-biased sample in the LSMO thin film at the STO interface which is not present in the not-exchange-biased system. These results provide microscopic experimental evidence of a nonmagnetic interfacial layer

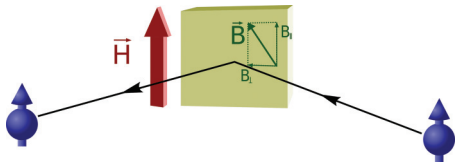

FIG. 1. (Color online) Scattering geometry of the PNR experiment. The up-up channel is shown, i.e., the spins of both the incoming and reflected neutrons, are oriented parallel to the applied magnetic field $\vec{H}$. $\vec{H}$ causes a magnetic induction $\vec{B}$ in the sample with two in-plane components $B_{\parallel}$ and $B_{\perp}$.

in the sample with oxygen deficiency. We argue that an antiferromagnetically ordered layer at the interface causes the observed EB effect.

II. EXPERIMENTAL

LSMO single layers and LSMO/STO bilayers have been grown by PLD and HSD in oxygen atmosphere on single-crystalline $SrTiO_3$ (001) substrates. Clean surfaces have been obtained by heating the substrates at a rate of 100 °C/h to 900 °C. After one hour at 900 °C, substrates have been cooled slowly to room temperature.

For the PLD growth, an excimer laser (Lambda LPX305) with wavelength 248 nm, a repetition rate of 10 Hz, and an energy density of 3.5 J/cm^2 were used. The cylindrical target consists of sintered powder with the nominal stoichiometry $La_{0.67}Sr_{0.33}MnO_3$ for the LSMO and a single-crystalline target for the $SrTiO_3$. A typical deposition rate of 0.6 nm/s was achieved for both materials. Substrates were placed on a resistive SiC heater. Deposition temperatures in the range of $T_s = 750$ °C were applied during the growth.

For the HSD sample preparation, commercial Lesker $La_{0.67}Sr_{0.33}MnO_3$ and $SrTiO_3$ targets with 2-inch diameter were used. LSMO was deposited by DC, and STO by AC sputtering, both at a deposition temperature of $T_s = 750$ °C. The oxygen pressure during sputtering was varied for different samples between 2.0 and 0.6 mbar.

The stoichiometry of the films, i.e., the ratios between La, Sr, and Mn, were analyzed employing Rutherford backscattering (RBS) with 1.4-MeV He^+ ions. X-ray reflectometry (XRR) was performed on a Bruker D8 reflectometer. Macroscopic magnetic characterization was carried out in a Quantum Design PPMS with a vibrating sample magnetometer (VSM) option.

PNR was performed on the magnetism reflectometer at the Spallation Neutron Source at Oak Ridge National Laboratory.[15] Data was taken in a 60-Hz time-of-flight mode using a wavelength band from 2 to 5 Å. A time-resolved two-dimensional position-sensitive detector was used to detect the reflected neutron beam at several incident angles. A Q range from 0 to 0.075 Å^{-1} was covered by combining the measurements at three different incident angles ($\theta = 0.2, 0.4$, and 0.8).

Figure 1 shows the geometry of the PNR experiment. An in-plane magnetic field $\vec{H}$ is applied to the sample, which causes a sample induction $\vec{B}$ with two in-plane components parallel ($B_{\parallel}$) and perpendicular ($B_{\perp}$) to $\vec{H}$. $\vec{H}$ also sets a quantization axis for the neutron beam that is reflected from the sample surface: the incoming neutron beam is polarized with the neutron spins oriented either parallel (up) or antiparallel (down) to the magnetic field.

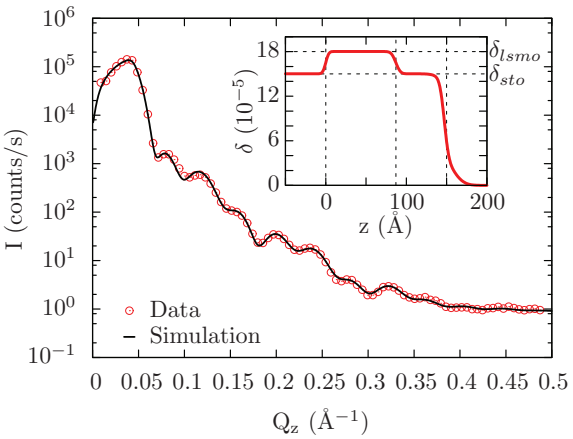

FIG. 2. (Color online) X-ray reflectivity of the exchanged-biased bilayer grown at 1.0 mbar at room temperature. Good agreement between measurement and simulation allows accurate LSMO and STO thickness determinations (87 and 63 Å, respectively). Inset: the resulting scattering length density profile of the simulation is shown, where δ is the refractive index decrement and z the distance from the surface of the substrate. The vertical dashed lines indicate the position of the interfaces of the bilayer. The horizontal dashed lines mark the bulk values of δ for LSMO and STO.

Similar to the x-ray reflectometry data analysis, Parratt's formalism was used to simulate the PNR data,[16] including a model to take interface roughnesses into account.[17] From the simulation of the PNR data, the nuclear (ρ_N) and magnetic (ρ_M) scattering length density profiles perpendicular to the sample surface were determined.

III. RESULTS

X-ray reflectivity data were modeled using Parratt's formalism.[16,18] Figure 2 shows one example of a measured x-ray reflectivity for a LSMO/STO bilayer prepared by sputtering. Using the scattering length densities of bulk LSMO and STO, layer thicknesses and roughnesses have been fitted to obtain a good agreement between data and simulation. It was necessary to introduce a thin surface layer (around 1 nm) with an additional roughness parameter to simulate the data, because the surface is not described well enough by a single rms roughness parameter. The resulting roughnesses for the layers are small, ranging between 0.5 and 1 nm, except for the LSMO single layers grown at 0.8 and 0.6 mbar, where they are slightly increased to 1.4 and 1.8 nm, respectively. A possible explanation is the slightly higher deposition rate for lower oxygen pressure. The determined thicknesses are listed in Table II.

Figure 3 gives an overview of the x-ray diffraction analysis of two LSMO single layers grown by HSD at 0.8 and 0.6 mbar. It can be seen that the (004) reflection of the film grown at 0.6 mbar is clearly shifted to smaller angles, corresponding to a larger out-of-plane lattice constant. The shifting of the out-of-plane lattice constants is well known for oxygen-deficient pseudocubic perovskites and has already been seen in LSMO,[19] and is usually explained by the change

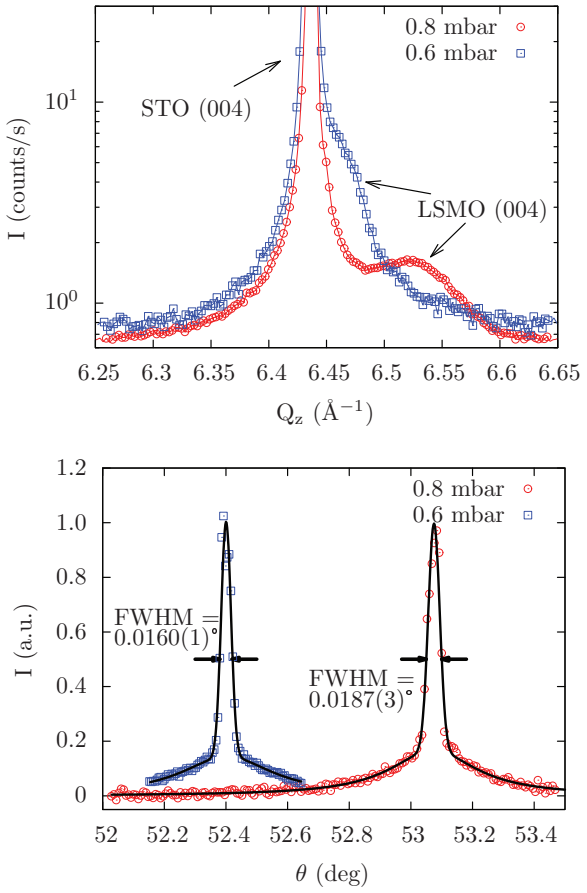

FIG. 3. (Color online) X-ray diffraction results: Comparison of the two single layers grown by HSD at 0.6 and 0.8 mbar. Top: $\theta/2\theta$ scans around the (004) reflections of STO and LSMO. Bottom: rocking curves of the (004) reflections of the LSMO films measured at $Q_z = 6.47$ (0.6 mbar) and $Q_z = 6.52$ (0.8 mbar), respectively. A detailed discussion on indication for strain relaxation deduced from these curves can be found in Ref. 21.

in the Mn^{3+} to Mn^{4+} ratio.[20] Nevertheless, the FWHM of the rocking curves measured of both samples are comparable, indicating that the structural quality of the samples should be very similar. The analysis of the bilayers cannot be done with this accuracy, since overlapping of LSMO and STO thickness oscillations inhibit the determination of the position of the LSMO reflection.

The macroscopic characterization was done by performing temperature scans from 5 to 340 K in a field of 0.5 mT during heating after cooling in a magnetic field of 1 T (Fig. 4). In addition, hysteresis curves have been measured at different temperatures. The Curie temperatures T_C have been estimated from the temperature scans by linear extrapolation of the magnetization to the abscissa. A strong dependence of T_C on the oxygen pressure during preparation is observed: for the PLD-grown samples and the sputtered samples grown at high oxygen pressure, T_C is approximately 320 K. With decreasing oxygen pressure during sample preparation, T_C decreases continuously down to about 57 K for the sample grown at 0.6 mbar (Fig. 4). Lower Curie temperatures are a well-known consequence of oxygen-deficient manganites.[22,23] In addition to the decreasing Curie temperature, the temperature-

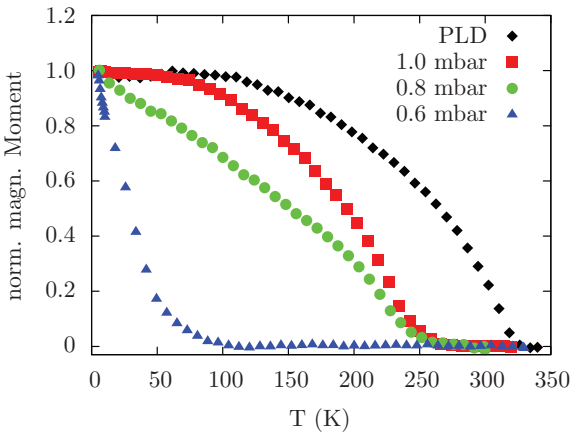

FIG. 4. (Color online) Temperature scans of the remanent magnetization at 0.5 mT after field cooling at 1 T of the samples analyzed by PNR. The magnetic moment has been normalized to the moment at 5 K. T_C drops significantly with decreasing oxygen pressure during growth.

dependent behavior below T_C for the samples grown at 0.8 and 0.6 mbar differ from typical ferromagnetic materials. Similar effects have been observed for oxygen-deficient $La_{1-x}Ca_xMnO_3$ films which revealed spin-glassy behavior.[23]

Even though the temperature-dependent behavior differs from standard ferromagnetic behavior for the samples grown at low oxygen pressures, all samples are clearly ferromagnetic below T_C: all samples show ferromagnetic hysteresis loops at low temperatures. Figure 5 compares the hysteresis curves at 5 K for the different samples measured after field cooling in +1 T. Two important results can be extracted from the hysteresis measurements. First of all we observe an increase of the coercive field H_C with decreasing oxygen pressure during sample growth from 5 mT for a sample grown by PLD to 119 mT for the sample grown by sputtering at an oxygen pressure of 0.6 mbar. This behavior is expected for oxygen-deficient LSMO and can be explained like the decreasing of the Curie temperature in the framework of not perfectly

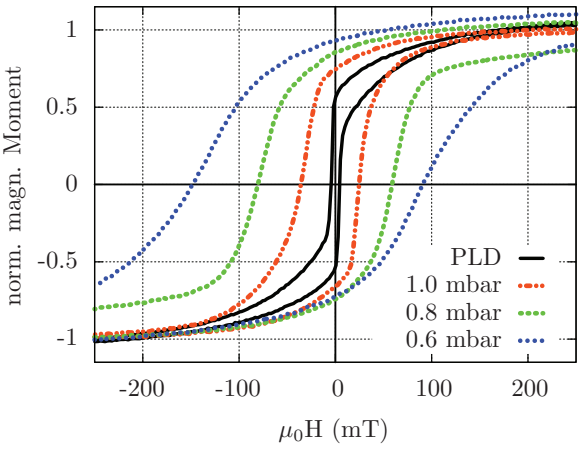

FIG. 5. (Color online) Hysteresis curves from samples at 5 K analyzed by PNR measured after field cooling at +1 T. The total field range was ±1 T (for better visibility, only the region between ±300 mT is shown). H_C and H_E values are listed in Table I.

TABLE I. Results of the VSM characterization: H_E–EB field, H_C–coercive field, and T_C–Curie temperature.

Pressure [mbar]	$\mu_0 H_E$ [mT]	$\mu_0 H_C$ [mT]	T_C [K]
PLD	0(1)	5(1)	320(2)
2.0	0(1)	5(1)	322(2)
1.2	0(1)	30(1)	277(2)
1.0	6(1)	31(1)	252(3)
0.8	7(1)	65(1)	249(3)
0.6	29(1)	119(1)	57(5)

homogeneous ferromagnets.[22] In addition, the PLD sample shows an unusual hysteresis, with a soft magnetic behavior at low field and slow approach to saturation with opening of the hysteresis at slightly higher fields. The second result is the presence of an exchange bias effect in the samples grown at oxygen pressures of 1 mbar or smaller. The samples grown at higher pressures and the PLD samples do not exhibit an EB effect. Similar to the coercive fields, the exchange bias field H_E, i.e., the shift of the hysteresis curves, becomes larger with decreasing oxygen pressure. It increases from 6 mT for the sample grown at 1 mbar to 29 mT for 0.6 mbar. Table I gives an overview of the results of the macroscopic magnetic characterization. Summarized, both the structural and the macroscopic characterization clearly indicate that oxygen deficiencies are present in the samples grown at lower pressures. Furthermore, we can control the amount of the deficiencies by adjusting the oxygen pressure. There is a strong dependence of the magnetic properties upon oxygen deficiency.

The macroscopic magnetic characterization of our thin-film samples containing nonmagnetic STO and (oxygen-deficient) nominally ferromagnetic LSMO indicates that an antiferromagnetic region, which causes the EB effect, should be present in the samples grown at lower pressures. Therefore we analyzed the magnetic depth profile of the LSMO/STO bi- and single layers by PNR to determine possible antiferromagnetic and ferromagnetic regions in our samples. As described earlier, we took R^+ and R^- reflectivities of the samples grown at 0.8 and 0.6 mbar and the PLD sample, at both 340 and 5 K. The high-temperature data was used to determine the nuclear scattering length densities (NSLDs) of the samples. Since the contrast between the NSLDs of STO and LSMO is very small (3.5×10^{-6} Å^{-2} and 3.7×10^{-6} Å^{-2}, respectively), there are no thickness oscillations visible above T_C. This is a huge advantage for our purpose, namely, to determine the magnetic depth profile accurately, since the low-temperature magnetic contrast between R^+ and R^- is not superimposed by chemical contrast between LSMO and STO. Hence, an accurate determination of the ferromagnetic layer thickness is possible.

The R^+ and R^- data taken at 5 K for the PLD bilayer together with the simulation of the data are depicted in Fig. 6. The resulting fit parameters are in very good agreement with the x-ray reflectometry results. Not only are the scattering length densities obtained by both methods in good agreement, but also the LSMO thickness determined by x-ray reflectometry matches perfectly with the ferromagnetic layer thickness determined by PNR (Table II), indicating that the complete LSMO layer is ordered ferromagnetically at 5 K. Furthermore, the magnetic scattering length density is only slightly smaller

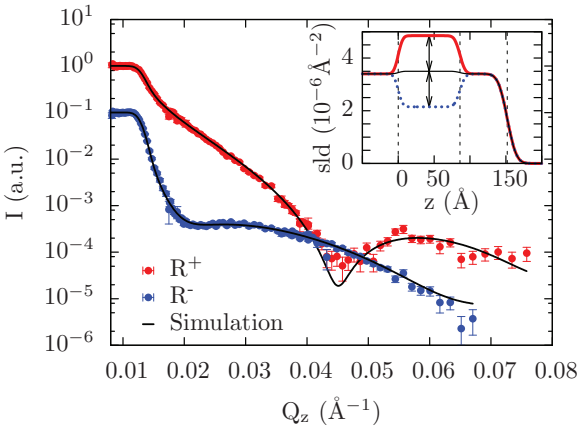

FIG. 6. (Color online) PNR of the LSMO/STO bilayer without EB measured at 6 K and in a saturation field of 1 T. R^- is divided by 10 for better visibility. Inset: The resulting scattering length density (*sld*) profile of the simulation is shown as a function of distance from the surface of the substrate z. The solid black line indicates the nuclear *sld* profile of the sample. Below the Curie temperature the magnetic *sld* of LSMO needs to be added to or subtracted from the nuclear *sld* to obtain the total *sld* of LSMO for the R^+ and R^- channels, respectively (solid red and blue lines). The vertical dashed lines indicate the position of the interfaces of the bilayer.

than the bulk value for $x = 0.33$ doped $La_{1-x}Sr_xMnO_3$, having a magnetic moment of $11/3\,\mu_B$ per unit cell.

In contrast to these results for the bilayer grown by PLD, the fit of the data for the single layer grown at 0.8 mbar results in a ferromagnetic layer thickness which is about 10 Å smaller than the LSMO thickness determined by x-ray reflectometry (95 and 105 Å, respectively). The data is shown in Fig. 7. The remaining part of the LSMO layer might have a small net magnetization (see last column in Table II) but will be called (macroscopically) nonmagnetic in the following. We also show the best possible fit for the case of a 105 Å ferromagnetic LSMO layer to point out the significant difference in our results. The data also reveals that the ferromagnetic layer is on top of the LSMO layer and

TABLE II. Summary of XRR and PNR. Listed are the LSMO layer thicknesses determined by XRR (d_{lsmo} Å), the thickness of the ferromagnetic region in LSMO determined by PNR at 5 K (d_{fm} Å), and the difference between both thicknesses, which gives the thickness of the region in the LSMO thin films of drastically reduced net magnetization (d_{NM} Å). Finally, the net magnetic moment per Mn atom of the ferromagnetic part (m_{fm}) and the interface region (m_{nm}) of the LSMO layer normalized to the bulk value for $x = 0.33$ Sr-doped LSMO ($m_{th} = 3.66\,\mu_B$). For comparison, the magnetic moment per Mn atom determined by VSM (m_{vsm}) is listed (calculated for a ferromagnetic LSMO layer having the thickness determined by PNR, not with the chemical layer thicknesses determined by XRR).

Pressure [mbar]	d_{lsmo} [Å]	d_{fm} [Å]	d_{nm} [Å]	m_{fm}/m_{th}	m_{nm}/m_{th}	m_{vsm}/m_{th}
PLD	85(2)	86(3)	−1(4)	0.91(6)	–	0.88(3)
0.8	105(1)	95(4)	10(5)	0.71(5)	0.1(1)	0.64(3)
0.6	177(2)	140(10)	37(12)	0.23(3)	0.04(5)	0.19(2)

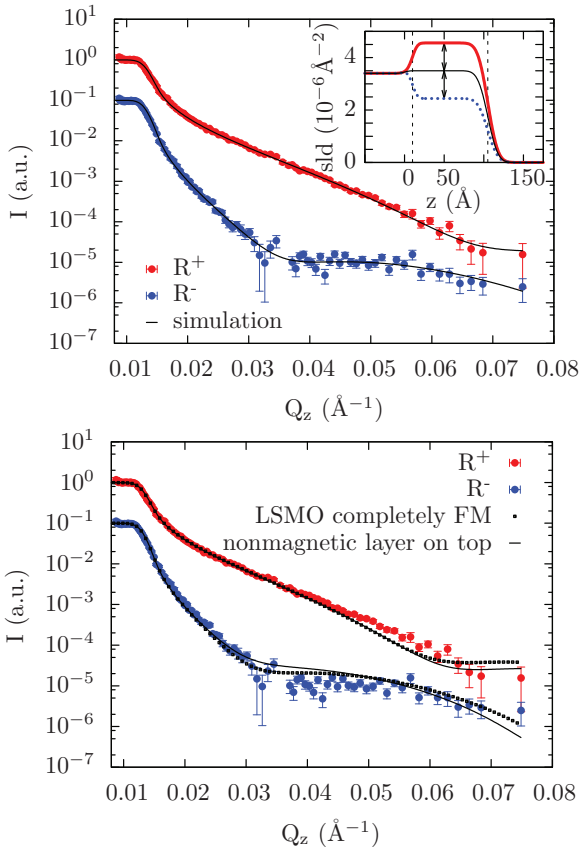

FIG. 7. (Color online) PNR of the LSMO single layer grown at 0.8 mbar. R^- is divided by 10 for better visibility. Top: Best fit to the data, giving a macroscopically nonmagnetic layer at the interface to the STO substrate. Bottom: Alternate simulations for the same sample. Best fit for a completely ferromagnetic LSMO layer and for a macroscopically nonmagnetic region at the surface of the LSMO layer. Inset: The resulting scattering length density (*sld*) profile of the simulation is shown as a function of distance from the surface of the substrate z. The solid black line indicates the nuclear *sld* profile of the sample. Below the Curie temperature the magnetic *sld* of LSMO needs to be added to or subtracted from the nuclear *sld* to obtain the total *sld* of LSMO for the R^+ and R^- channels, respectively (solid red and blue lines). The vertical dashed lines indicate the position of the magnetic interfaces of the single layer. Note that the position of the magnetic interface to the substrate is shifted with respect to the chemical interface at $z = 0$, indicating a region of drastically reduced magnetization at the LSMO/STO interface.

the nonmagnetic layer at the interface to the STO substrate. The other way around, i.e., a nonmagnetic layer on top of a 95-Å ferromagnetic layer of LSMO, leads to a clearly worse simulation compared to the observation. The significance of our results can be underscored by comparing the figure of merits ($FOM = \frac{1}{N}\sum_i^N [\log(D_i) - \log(S_i)]^2$, where D_i are the N experimental intensity data points and S_i the corresponding simulated values) for the different solutions: whereas the FOM is 6.64 for the best fit, it is more than two times larger in the case of a completely ferromagnetic LSMO layer or a nonmagnetic layer on top of the LSMO layer (13.7 and 16.0, respectively). The effect is more pronounced for the sample grown at 0.6 mbar: compared to a LSMO layer thickness of 177 Å, the PNR data give a ferromagnetic layer thickness of 140 Å again on top of the single layer, leaving a 37-Å nonmagnetic layer at the STO interface. The thicknesses of the nonmagnetic LSMO region listed in Table II are not determined by the PNR data fit. Due to the small difference in the NSLDs of STO and LSMO, one can hardly see the interface between the substrate and the nonmagnetic LSMO. Thus the thickness of the nonmagnetic region can be chosen almost arbitrarily in the PNR simulations. Instead the thickness listed in the table is the difference between the LSMO layer determined by x-ray reflectometry and the thickness of the ferromagnetic LSMO layer determined by PNR. In addition to the increasing nonmagnetic LSMO layer thickness with decreasing oxygen pressure during preparation, the magnetic scattering length densities of the ferromagnetic part of the LSMO layers also are smaller than for the bilayer without EB effect (71% and 23% for the samples grown at 0.8 and 0.6 mbar, respectively), which again is expected for oxygen-deficient LSMO thin films.[22] The resulting magnetic moments per Mn atom determined by PNR are in very good agreement with the values obtained by the macroscopic magnetization measurements for all the samples.

IV. DISCUSSION

The combination of the macroscopic magnetic characterization and PNR measurements leads us to the following interpretation. The PNR measurements reveal regions with strongly suppressed, maybe even vanishing net magnetization of LSMO at the interface to STO. Since reflectometry does not resolve the magnetic structure on an atomic length scale, this "nonmagnetic" region can in fact be ordered antiferromagnetically. In this case, a ferromagnetic (FM)–antiferromagnetic (AFM) interface is present in the samples with oxygen-deficient LSMO layers, which then causes the EB effect. The occurrence of the EB effect in our samples can be understood by generalizing the well-known strain-doping phase diagram of LSMO, which has been proposed experimentally by Konishi *et al.*[24] and theoretically by Fang *et al.*[25] (Fig. 8).

The structural characterization by x-ray scattering and also the VSM measurements clearly indicate oxygen deficiencies in the LSMO layer. Furthermore, we can adjust the oxygen content by varying the oxygen pressure. Effectively, this leads to the same result as changing the La/Sr ratio to a lower Sr content in the LSMO layer when the Mn^{4+} content and thus the charge-carrier density is decreased. According to the oxygen vacancy model,[26,27] the resulting Mn^{4+} content can be calculated by the following chemical formula:

$$La_{1-x}Sr_xMn^{3+}_{1-x+2\delta}Mn^{4+}_{x-2\delta}O_{3-\delta}. \quad (1)$$

Hence, oxygen vacancies result in a shift in the phase diagram in Fig. 8 to the left, even though x might still equal 0.33. This effect alone seems insufficient in our samples to reach the AFM region, as there is a ferromagnetic order for the majority of the LSMO layer. But at the interface, in addition to the change in charge-carrier density, we also have a compressive strain mediated by the STO substrate which is equivalent to a shift in the diagram downwards. To the best of our knowledge, there are neither theoretical calculations nor experimental reports on a strain phase diagram for doping levels smaller

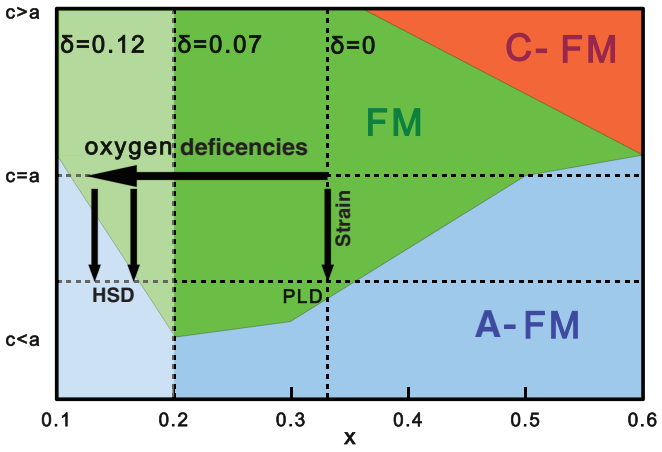

FIG. 8. (Color online) Schematic strain vs doping phase diagram of LSMO. The information for the doping range between $x = 0.2$ and $x = 0.6$ is taken from Refs. 25 and 24. The phase boundary between the FM and A-AFM region for a doping level smaller then 0.2 is an assumption or rather an interpolation between the last calculated point in Ref. 25 for $x = 0.2$ and the known fact that bulk LSMO with $x = 0.1$ exhibits the A-AFM structure (Ref. 8). Even though the doping level is kept at 0.33 for the samples under investigation, one can still "move" through the phase diagram by oxygen deficiencies (according to formula (1)) and strain and reach the A-AFM region. The δ values give the necessary oxygen deficiency to reach the same Mn^{4+}/Mn^{3+} ratio as a fully oxygenated LSMO with a doping level at the corresponding position.

than 0.2. However, it is well known for bulk LSMO that for doping levels smaller than 0.16 the antiferromagnetic A-type structure (A-AFM) is established.[8] By combining this information with the calculations and experimental data for larger doping levels, one can assume that the phase diagram between $x = 0.1$ and 0.2 looks qualitatively as shown in Fig. 8. In this case, a combination of oxygen deficiency and compressive strain can result in an antiferromagnetic order at the STO interface. After relaxation a ferromagnetic order is established in the rest of the layer. This interpretation can only be valid if the samples exhibiting an EB effect have an oxygen deficiency large enough to result in a Mn^{4+}/Mn^{3+} ratio smaller than 0.25 (which corresponds to a Sr doping of $x = 0.2$ for fully oxidized LSMO), as for larger Mn^{4+}/Mn^{3+} ratios a bigger strain than for the fully oxidized LSMO with $x = 0.33$ is needed in order to reach the A-AFM phase (see phase diagram between $x = 0.2$ and $x = 0.33$). Therefore, according to formula (1) an oxygen deficiency larger than $\delta = 0.07$ is needed. The fact, that the antiferromagnetic layer gets thicker with increasing oxygen deficiencies also supports the assumption that the oxygen deficiencies are in the range between $\delta = 0.07$ and 0.1; in this region a sample with higher oxygen deficiencies needs a smaller strain to reach the AFM phase. Therefore at the LSMO/STO interface, a region at a certain strain, which is ordered ferromagnetically in the sample grown at 0.8 mbar, might be still ordered antiferromagnetically at the same strain in the sample grown at 0.6 mbar due to the larger oxygen deficiency. Thereby, for the sample grown at 0.6 mbar a bigger relaxation layer is needed to end up in the FM region, resulting in a thicker AFM interfacial layer. To finally proof this interpretation, a more detailed analysis of the relaxation process in the samples and the corresponding length scale it occurs needs to be done. Some indication for the strain relaxation has been extracted from the x-ray diffraction data,[21] and at least for the single layer grown at 0.6 mbar the thickness of the strained region is very similar to the thickness of the AFM region (about 30–40 Å). Another way of proving our interpretation would be the investigation of multilayers by neutron diffraction; magnetic reflections caused by an antiferromagnetic order could be detected by this method. Neutron diffraction is not possible for the samples discussed here, as the diffracted intensity would be too small.

It is important to note that since the EB effect is purely due to the LSMO layer and the STO substrate is only needed to mediate the strain, one is not limited to having to chose an antiferromagnet on one side and a ferromagnet on the other side of the chemical interface to create an EB effect. This opens up the opportunity of choosing the second material independently, as long as it sets the right strain to the magnetic layer. As in our case, one layer need not to be magnetic at all but could have other properties, which possibly creates completely new and more versatile functionalities.

V. CONCLUSION

We have prepared a set of LSMO single layers and LSMO/STO bilayers by HSD and PLD. We show that we can influence the oxygen stoichiometry by changing the oxygen pressure in the HSD chamber during deposition. The detection of an EB effect in the oxygen-deficient LSMO layers indicates that an antiferromagnetically ordered region is present in the samples. We detect a layer with drastically reduced or maybe even no net magnetization at the interface to the STO substrates, where the LSMO most likely orders antiferromagnetically. We present a possible scenario as an explanation for the EB effect by a combination of oxygen deficiencies and strain at the STO interface. Our observation opens up possibilities in tailoring the properties of thin-film oxides: since the EB is caused by one material only, the second material can be chosen to be nonmagnetic, as long as it sets the right strain. Therefore one could think of using materials having properties that might couple and influence the EB material and hence create new versatile material systems.

[1] J. Heber, Nature (London) **459**, 28 (2009).
[2] A.-M. Haghiri-Gosnet and J.-P. Renard, J. Phys. D: Appl. Phys. **36**, R127 (2003).
[3] J. G. Bednorz and K. A. Müller, Z. Phys. B: Condens. Matter **64**, 189 (1986).
[4] W. H. Meiklejohn and C. P. Bean, Phys. Rev. **102**, 1413 (1956).
[5] A. E. Berkowitz and K. Takano, J. Magn. Magn. Mater. **200**, 552 (1999).
[6] J. Nogues and K. Schuller, J. Magn. Magn. Mater. **192**, 203 (1999).

[7]S. M. Wu, S. A. Cybart, P. Yu, M. D. Rossell, J. X. Zhang, R. Ramesh, and R. C. Dynes, Nat. Mater. **9**, 756 (2010).
[8]J. Hemberger, A. Krimmel, T. Kurz, H.-A. Krug von Nidda, V. Yu. Ivanov, A. A. Mukhin, A. M. Balbashov, and A. Loidl, Phys. Rev. B **66**, 094410 (2002).
[9]A. Tebano, C. Aruta, P. G. Medaglia, F. Tozzi, G. Balestrino, A. A. Sidorenko, G. Allodi, R. De Renzi, G. Ghiringhelli, C. Dallera, L. Braicovich, and N. B. Brookes, Phys. Rev. B **74**, 245116 (2006).
[10]J.-S. Lee, D. A. Arena, P. Yu, C. S. Nelson, R. Fan, C. J. Kinane, S. Langridge, M. D. Rossell, R. Ramesh, and C.-C. Kao, Phys. Rev. Lett. **105**, 257204 (2010).
[11]H. F. Li, Y. Su, J. Persson, P. Meuffels, J. M. Walter, R. Skowronek, and Th. Brückel, J. Phys.: Condens. Matter **19**, 016003 (2007).
[12]S. J. Zhu, J. Yuan, B. Y. Zhu, F. C. Zhang, B. Xu, L. X. Cao, X. G. Qiu, B. R. Zhao, and P. X. Zhang, Appl. Phys. Lett. **90**, 112502 (2007).
[13]S. J. Zhu, B. R. Zhao, B. Y. Zhu, B. Xu, L. X. Cao, and X. G. Qiu, Appl. Phys. Lett. **91**, 012505 (2007).
[14]S. J. Zhu, B. R. Zhao, B. Xu, B. Y. Zhu, L. X. Cao, and X. G. Qiu, J. Phys. D: Appl. Phys. **41**, 215007 (2008).
[15]V. Lauter, H. Ambaye, R. Goyette, W.-T. Hal Lee, and A. Parizzi, Physica B **404**, 2543 (2009).
[16]L. G. Parratt, Phys. Rev. **95**, 359 (1954).
[17]E. Kentzinger, U. Rücker, B. Toperverg, F. Ott, and Th. Brückel, Phys. Rev. B **77**, 104435 (2008).
[18]J. Stettner, Ph.D. thesis, Christian-Albrechts-Universität zu Kiel, 1995.
[19]J. Li, J. M. Liu, H. P. Li, H. C. Fang, and C. K. Ong, J. Magn. Magn. Mater. **202**, 285 (1999).
[20]H. L. Ju, J. Gopalakrishnan, J. L. Peng, Qi Li, G. C. Xiong, T. Venkatesan, and R. L. Greene, Phys. Rev. B **51**, 6143 (1995).
[21]D. Schumacher, Ph.D. thesis, RWTH Aachen, 2013.
[22]H. L. Ju and H. Sohn, J. Magn. Magn. Mater. **167**, 200 (1997).
[23]Z. Fu-Chang, C. Wei-Ran, G. Wei-Zhi, X. Bo, Q. Xiang-Gang, and Z. Bai-Ru, Chin. Phys. **13**, 783 (2004).
[24]Y. Konishi, Z. Fang, M. Izumi, T. Manako, M. Kasai, H. Kuwahara, M. Kawasaki, K. Terakura, and Y. Tokura, J. Phys. Soc. Jpn. **68**, 3790 (1999).
[25]Z. Fang, I. V. Solovyev, and K. Terakura, Phys. Rev. Lett. **84**, 3169 (2000).
[26]S. Madhukar, S. Aggarwal, A. M. Dhote, R. Ramesh, A. Krishnan, D. Keeble, and E. Poindexter, J. Appl. Phys. **81**, 3543 (1997).
[27]A. N. Petrov, V. A. Cherepanov, O. F. Kononchuk, and L. Ya. Gavrilova, J. Solid State Chem. **87**, 69 (1990).